LAWRENCE
LIVERMORE
NATIONAL
LABORATORY

LLNL-BOOK-409734

High-resolution architecture and structural dynamics of microbial and cellular system: Insights from high-resolution in vitro atomic force microscopy

A.J. Malkin, M. Plomp

January 9, 2009

Scanning Probe Microscopy of Functional Materials: Nanoscale Imaging and Spectroscopy

Disclaimer

Chapter for the book entitled *"Scanning Probe Microscopy of Functional Materials: Nanoscale Imaging and Spectroscopy"* (Eds. S.V. Kalinin and A. Gruverman). To be published by Springer in 2009

High-resolution architecture and structural dynamics of microbial and cellular system: Insights from high-resolution in vitro atomic force microscopy.

Alexander J. Malkin* and Marco Plomp

Physical and Life Sciences Directorate, Lawrence Livermore National Laboratory,

Livermore CA 94551, USA

* Corresponding author: Mailing address: Physical and Life Sciences Directorate, L-234,

Lawrence Livermore National Laboratory, 7000 East Avenue, Livermore CA 94551.

Phone: (925) 423-7817; FAX: (925) 422-2041. E-mail: **malkin1@llnl.gov**

Introduction

One of the great scientific challenges at the intersection of chemistry, biology and materials science is to define the biophysical pathways of cellular life, and in particular, to elucidate the complex molecular machines that carry out cellular and microbial function and propagate the disease. To study this in a comprehensive way, the fundamental understanding of the principal mechanisms by which cellular systems are ultimately linked with their chemical, physical and biological environment are required. Complete genome sequences are often available for understanding biotransformation, environmental resistance and pathogenesis of microbial and cellular systems. The present technological and scientific challenges are to unravel the relationships between the organization and function of protein complexes at cell, microbial and pathogens surfaces, to understand how these complexes evolve during the bacterial, cellular and pathogen life cycles, and how they respond to environmental changes, chemical stimulants and therapeutics. Development of atomic force microscopy (AFM) for probing the architecture and assembly of single microbial surfaces at a nanometer scale under native conditions, and unraveling of its structural dynamics in response to changes in the environment has the capacity to significantly enhance the current insight into molecular architecture, structural and environmental variability of cellular and microbial systems as a function of spatial, developmental and temporal organizational scales.

In this chapter we will demonstrate, focusing on the work conducted in our group in the past several years, the capabilities of AFM in probing the architecture and assembly of bacterial surfaces and integument structures and their evolvement during bacterial life cycles, as well as in response to environmental changes. We have used AFM to investigate spore coat architecture and assembly, structural dynamics and germination of several species of *Bacillus*[1-7]and *Clostridium*[8] spores. These include *Bacillus thuringiensis, Bacillus anthracis, Bacillus cereus, Bacillus atrophaeus and Clostridium novyi-NT spore species. B. anthracis,* the causative agent of anthrax, is a Gram-positive spore forming bacterium.[9,10] The *B. cereus* species is environmentally ubiquitous and can cause bacterimia and septicemia, central nervous and respiratory system infections, endocarditis and food poisoning.[11] *B. atrophaeus* spores have been used as a biological stimulant for decontamination and sterilization processes,[12,13] and bioaerosol detection development.[14,15] The *B. thuringiensis* spores are the insect pathogenic species.[16] *Clostridium novyi* (*C. novyi-NT*) is a motile, spore-forming, Gram-variable anaerobic bacterium. *C. novyi* can cause infections leading to gas gangrene in humans, particularly after traumatic wounds or illicit drug use.[17] The pathology of *C. novyi* is attributed to the lethal alpha-toxin,[18] which is absent in an attenuated strain, *C. novyi-NT*.[19] *C. novyi-NT* is one of the most promising bacterial agents for cancer therapeutics.[20] Intravenous injection of *C. novyi-NT* spores into tumor-bearing mice was found to successfully eradicate large tumors, either in combination with radiation therapy[19] and chemotherapy,[21] or by itself, as it can induce a potent immune response.[22]

Here, we will also describe the development of AFM for immunolabeling of the proteomic structures of bacterial spore surfaces.[5] Finally, we will present data on the

elucidation of bioremediation mechanisms of *Arthrobacter oxydans*. *A. oxydans* is a gram-positive and chromium (VI)-resistant bacterium, which can reduce highly mobile, carcinogenic, mutagenic, and toxic hexavalent chromium to less mobile and much less toxic trivalent chromium.[23]

AFM investigations of spore morphology, structural dynamics and spore coat architecture.

When starved for nutrients *Bacillus* and *Clostridium* cells initiate a series of genetic, biochemical and structural events that results in the formation of a metabolically dormant endospore.[24] Bacterial spores can remain dormant for extended time periods and possess a remarkable resistance to environmental insults, including heat, radiation, pH extremes and toxic chemicals.[24] Their unique structure, including a set of protective outer layers, plays a major role in the maintenance of spore environmental resistance and dormancy.[24-26] The *Bacillus* bacterial spore structure (Fig. 1a) consists,[25] starting from the center, of an inner core surrounded by the inner cytomembrane, a cortex, outer membrane and an

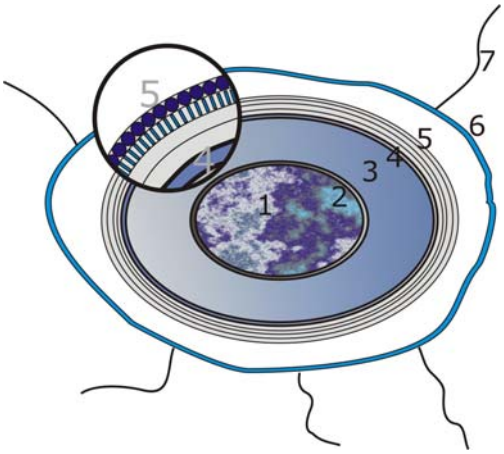

Figure 1. Structure of a *Bacillus* spore: spore core (1); inner membrane (2); cortex (3); outer membrane (4); spore coat (5); exosporium (6) and appendages (7). Insert: spore coat with two crystalline layers of the outer spore coat.

exterior spore coat. In some bacterial species, including *Bacillus thuringiensis* and *Bacillus anthracis*, the coat is surrounded by a loosely attached exosporium. The spore

core contains DNA and dipicolinic acid, which is associated predominantly with Ca^{2+}. The major role of the spore cortex, which consists of a thick layer of species-dependent peptidoglycan, is to maintain spore heat resistance and dormancy.[25]

***Bacillus* and *Clostritium* spore morphology**. AFM images of various species of air-dried *Bacillus* and *Clostridium-NT* spores are presented in Fig. 2. As illustrated in Fig.2, *B. thuringiensis, B. cereus* and *B. anthracis* native spores are enclosed within an exosporium sacculus (indicated with the letter *E* in Fig. 1a-d), which is larger than the dimensions of the spore body for two former species (Fig.1a, Fig.1c) and often tightly attached to the spore coat in the case of *B. anthracis* spores (Fig. 1d).

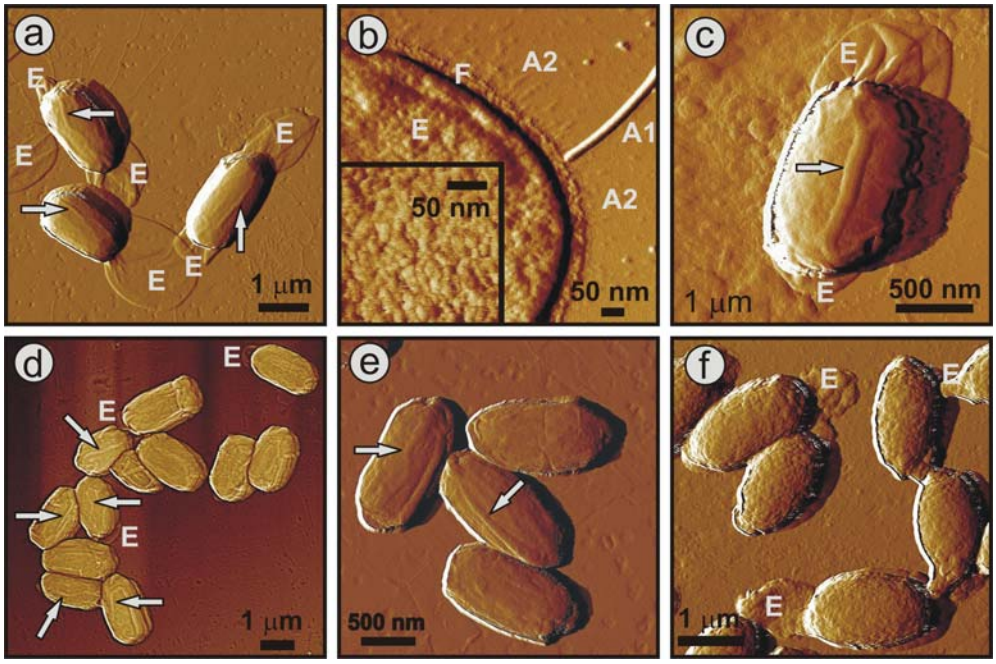

Figure 2. AFM images of air-dried bacterial spores. (a,b) *B. thuringiensis*, (c) *B. cereus,* (d), *B. anthracis* (e) *B.atrophaes*, and (f) *C. novyyi-NT* spores. In (b) AFM image of the *B. thuringiensis* exosporium showing a footstep (F) with numerous hair-like appendages (A2) and longer and thicker tubular appendage (A1). Surface ridges, extending along the

entire spore length are indicated with white arrows in (a) and (c-e). Exosporium is indicated with E in (a-d). "Shell tail" in (f) is indicated with S.

Comment [AM1]: Replace E with S in (f)

The major part of the exposporium is reported to consist of two glycoprotein components[27,28] and significant amounts of lipid (18%) and carbohydrate (20%), and smaller amounts of other components including amino sugars.[29,30] It is constructed out of an inner part with 3-4 thin hexagonal crystalline layers, and an amorphous, hirsute layer on the outside.[31,32] For *B. anthracis* spores, the exosporium is composed of a paracrystal basal layer and an external hair-like nap layer extending up to 600 nm in length[33] with approximately 20 exosporium-associated protein and glycoprotein species being identified.[33-36] The thickness of substrate-bound exosporium patches and of the hirsute layer as measured from the AFM height data (Fig. 1) varied in the range 15-25 nm and 30-35 nm respectively[1,2], which corresponds with earlier EM measurements.[31,32].

Apart from the 30-35 nm hirsute layer, the exosporium surface is frequently decorated with surface appendages.[37-39] These structures are most often described as hollow tubular filamentous extensions similar to pili of enterobacteria. The reported dimensions are variable but are in the range of 0.03 to 0.6 µm in width and 1.5 to 3.0 µm in length. These structures are most frequently described in the closely related *B. cereus*, *B. anthracis* and *B. thuringiensis* group. The number of appendages per spore varies from three to more than twenty. It is not clear in the case of *Bacillus* spores if appendages originate on the spore coat or exosporium. These filaments could be of importance for spore attachment to surfaces or ligands. As illustrated in Fig. 1b, the filamentous exosporial appendages appeared to be attached to the outer surface of the exosporium. Two types of appendages were typically observed. The first type (indicated as A1)

appeared to be tubular with a diameter and length in the range of 8-12 nm and 400-1200 nm respectively. Other appendages, such as those indicated as A2 in Fig. 1b, were 2.5-3.5 nm thick and typically 200-1600 nm long. Six to ten appendages were seen on the exosporium surface.

B. atrophaeus spores (Fig. 1e) do not possess exosporia, with the outer spore coat being the outermost surface. As illustrated in Fig. 1f, *C. novyi-NT* spores were encased in amorphous shells. Many spores exhibited ~ 200 nm thick shell 'tails' at their poles (Fig. 2a, b) similar to 'tails' visualized by EM.[8] High-resolution AFM images reveal that the outer shell surface typically consists of irregular amorphous material.[8]

The most pronounced morphological features seen on the surfaces of air-dried *Bacillus* spores are ridges (indicated on several spores with arrows in Fig.1), which typically extend along the long axis. Thickness of the ridges typically varies from 20-60 nm. Similar ridges were previously reported by electron microscopy[40] and AFM studies of various species of bacterial spores. [1-3,41]

Spore size distributions. The interspecies distributions of spore length and width were determined for four species of *Bacillus* spores in aqueous and aerial phases (Fig.3). It was found[1] that the dimensions of individual spores differ significantly depending upon species, growth regimes and environmental conditions. Spores of *B. thuringiensis* are substantially larger (~50% higher and ~20% longer) than *B. atrophaeus* and *B. subtilis* spores. The difference in average width and length between plate-grown and solution-grown spores of *B. atrophaeus* and *B. thuringiensis* suggest that environmental/physiological factors can have significant effects on spore dimensions.

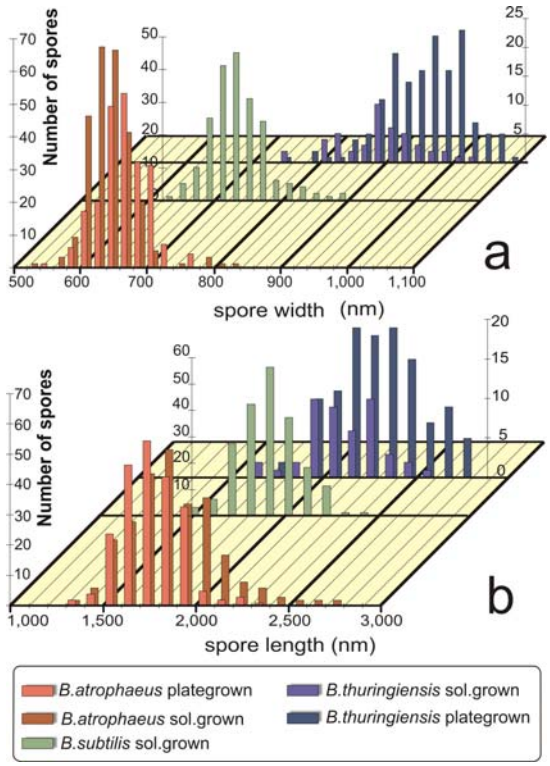

Figure 3. Distribution of spore width (a) and length (b) for plate-grown (pg) and solution-grown (sg) *B. atrophaeus* and *B. thuringiensis* spores, and solution-grown *B. subtilis* spores.

Comment [AM2]: Let's use here Figure 3 from Biophys. J. Could you please make lettering etc consistent with other figures. We don't need stars indicating average sizes

These findings could be useful in the reconstruction of environmental/preparation conditions during spore formation and for modeling the inhalation and dispersal of spores.

Spore Response to a Change in the Environment from Fully Hydrated to Air-Dried State. AFM allows, for the first time, a direct comparison of fully hydrated and air-dried native spores visualized under water and in air, respectively.[1] Images of fully hydrated *B. atrophaeus* spores are presented in Fig. 4. Surface ridges, the prominent structural features of air-dried spores (Fig. 1), are typically absent from the surface of fully hydrated spores (Fig. 5a), with shallow 5-15 nm thick surface wrinkles occasionally present. Apparently, the spore coat of the fully hydrated spore is tightly attached to the underlying cortical integument.

The surface morphology of fully hydrated and air-dried spores spans a wide range of folding motifs (Figs. 1 and 4). Therefore, direct visualization of *individual* spores is

required in order to probe the dynamic response of this aqueous to aerial phase transition. This analysis was performed for 35 individual spores.[1] Spores were visualized under water, then air-dried for ~ 40 hours, imaged in air (65% relative humidity), and reimaged after rehydration. Typical examples of hydration/dehydration ultrastructural transitions

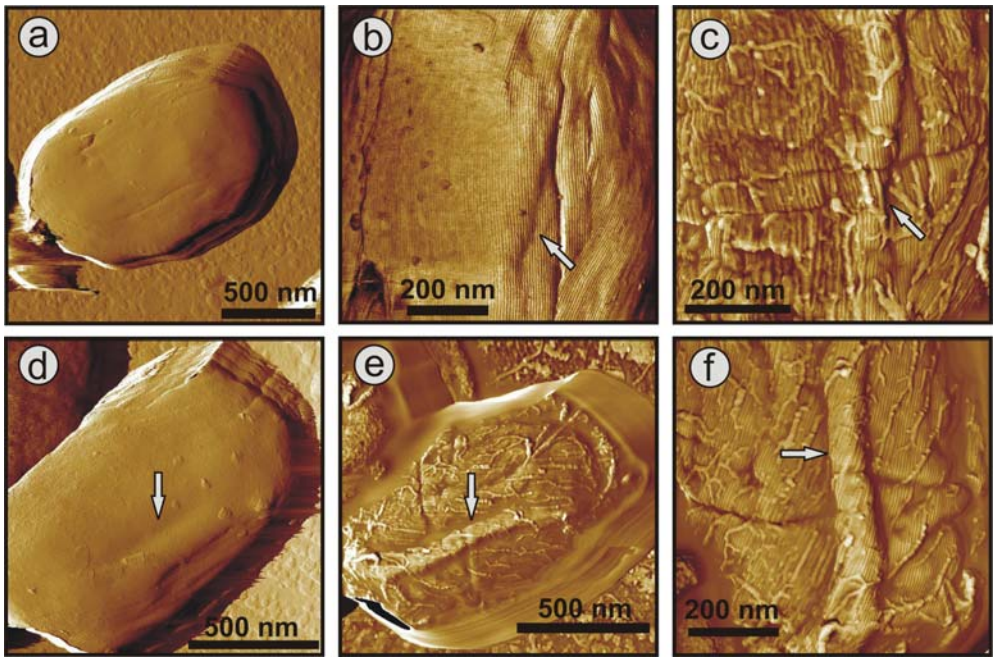

Figure 4. AFM images showing the dynamic response of *B. atrophaeus* spores to dehydration. (a) Spore coat surface morphology of a fully hydrated spore. The area indicated with a square in (a) is shown at high resolution in (b). A shallow wrinkle on the surface is indicated in (b) with an arrow. In (c) the same area is shown after air-drying. The wrinkle seen in (b) developed into a fold/surface ridge (indicated with white arrow) with increased height and length. Structural alterations are seen in the surfaces morphology of a hydrated spore (d) and after air-drying (e). Formation of a surface ridge (indicated with an arrow) is seen in (e) and at higher resolution in (f) along with the emergence of a number of smaller folds.

are presented in Fig. 4. As illustrated in Figure 4a, the spore coat of a fully hydrated spore appears to be tightly attached to the cortex, excluding an area with an ~600 nm long wrinkle having a height of ~ 15-20 nm (Fig. 4a,b). Upon dehydration (Fig.4c) this wrinkle becomes a surface ridge/fold extending along the entire length of the spore, accompanied by a height increase of ~ 50 nm.

Similarly, the surface of another fully hydrated spore (Fig. 1d), exhibits a ~ 500 nm long fold (indicated with an arrow) having a height of ~ 30 nm. Upon dehydration, a new ~ 800nm long surface ridge/fold (indicated with white arrow in Fig. 4e), having a height of ~40-60 nm and a number of smaller folds with a height range of ~10-30 nm, forms on the spore coat.

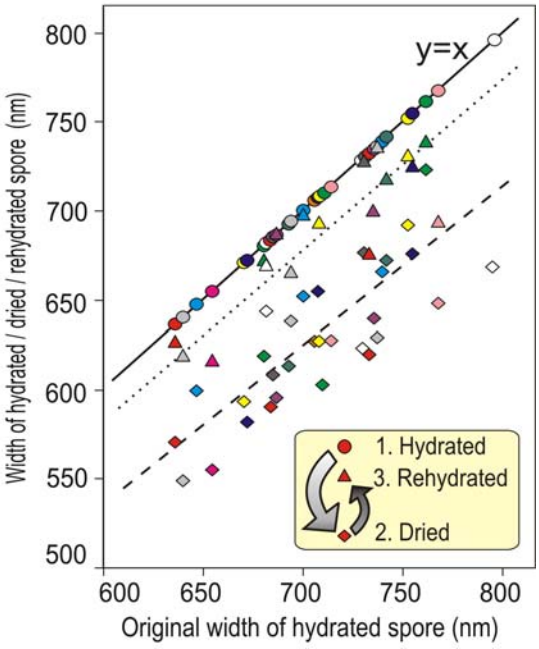

These profound dehydration induced changes in spore surface architecture were found to be accompanied by a pronounced decrease in spore size. As illustrated in Fig. 5, the average width of 35 individual air-dried spores was reduced to

Figure 5. Spore width variations of 35 individual *B. atrophaeus* spores, as a function of the size of the originally hydrated spore, following dehydration (24 hrs) (diamonds, dashed trend line) and rehydration (2 hours) (triangles, dotted trend line). For ease of comparison, the original hydrated spore width is (redundantly) depicted as circles, which by definition lie on the solid $y=x$ line. Thus, the three data points for one individual spore, depicted with the same color, are all on the same vertical line. Several spores detached from a substrate during rehydration experiments resulting in a smaller amount of experimental rehydration points (triangles).

88% of the size measured for fully hydrated spores. Upon re-hydration of air-dried spores, they returned to 97% of their original size after 2 hrs in water, establishing the reversibility of the size transition (Fig. 5).

The results from these individual spore measurements were confirmed by independent experiments (not presented here) where *B. atrophaeus* spore width was measured for two independent sets of ~200 spores in water and air, respectively. The width of the air-dried spore was again reduced to ~ 88% when compared to spores imaged in water.

The observed decrease in the width of bacterial spores upon dehydration is apparently due to the contraction of the spore core and/or cortex. The ability of the coat to fold and unfold concomitant with changes in spore size was suggested[1,41,42] based on measurements of *B. thuringiensis* spore dimensions induced by humidity transients.[43] First direct visualization[1] of the response of native spores to dehydration/rehydration described above clearly demonstrates, that the spore coat is itself does not shrink/expand but is flexible enough to compensate for the internal volume decrease of core/cortex compartments by surface folding and formation of ridges. These studies establish that the dormant spore is a dynamic physical structure.

The observed folding could involve either the outer coat layer or the entire ensemble of inner and outer coat layers. In case *of B. atrophaeus*, if only the outermost rodlet layer (Fig. 4) was exclusively involved in folding, then due to the highly anisotropic rodlet structures, folding would most likely take place preferentially along the orientation of the rodlets. However, as seen in Fig.4 folding of the coat takes place in arbitrary orientations with respect to the rodlet structures. This suggests that the whole spore coat folds with the

inner surface of the coat disconnecting locally from the outer surface of the spore cortex. A number of ridges vary broadly for different *Bacillus* species. Thus the outer coat of *B. thuringiensis* spores typically exhibited less ridge formation when compared with *B. atrophaeus* and *B. cereus* spores. This finding suggests that the outer spore coat elastic properties may vary among spore-forming species.

High-resolution structure and assembly of the spore coat. The multilayer spore coat (Fig. 1) consists of structural proteins and small amounts of carbohydrate.[24-26] The spore coat plays an important role in spore protection and germination. Approximately 50 *Bacillus* spore coat proteins or coat protein orthologs have been identified by genomic and proteomic analysis.[24-26,44] Despite the recent advances in biochemical and genetic studies,[44] spore coat morphogenesis, which includes self-assembly of crystalline layers of the spore coat, is still poorly understood. In particular, it is not clear which spore coat proteins form various spore coat layers, what their roles in the coat assembly, and which proteins are surface-exposed and which ones are embedded beneath the surface.

The elucidation of bacterial spore surface architecture and structure-function relationships is critical to determining mechanisms of pathogenesis, environmental resistance, immune response, and associated physicochemical properties. Thus, the development and application of high-resolution imaging techniques, which could address spatially explicit bacterial spore coat protein architecture at nanometer resolution under physiological conditions, is of considerable importance.

We have directly visualized species-specific high-resolution native spore coat structures of bacterial spores including the exosporium and crystalline layers of the spore

coat (Fig.1) of various *Bacillus*[1-4,6,7] and *Clostridium novyi-NT*[8] species in their natural environment, namely air and fluid.

For *B. atrophaeus* (Fig.6a,b), and *B. subtilis* spores (data not shown here), the outer spore coat was composed of a crystalline rodlet layer with a periodicity of ~ 8 nm. Removal of the *B. cereus* and *B. thuringiensis* exosporium by sonication[1] or single cell French Press treatment[8] revealed crystalline rodlet (Fig. 1c) and hexagonal honeycomb (Fig. 1e) outer spore coat structures respectively.

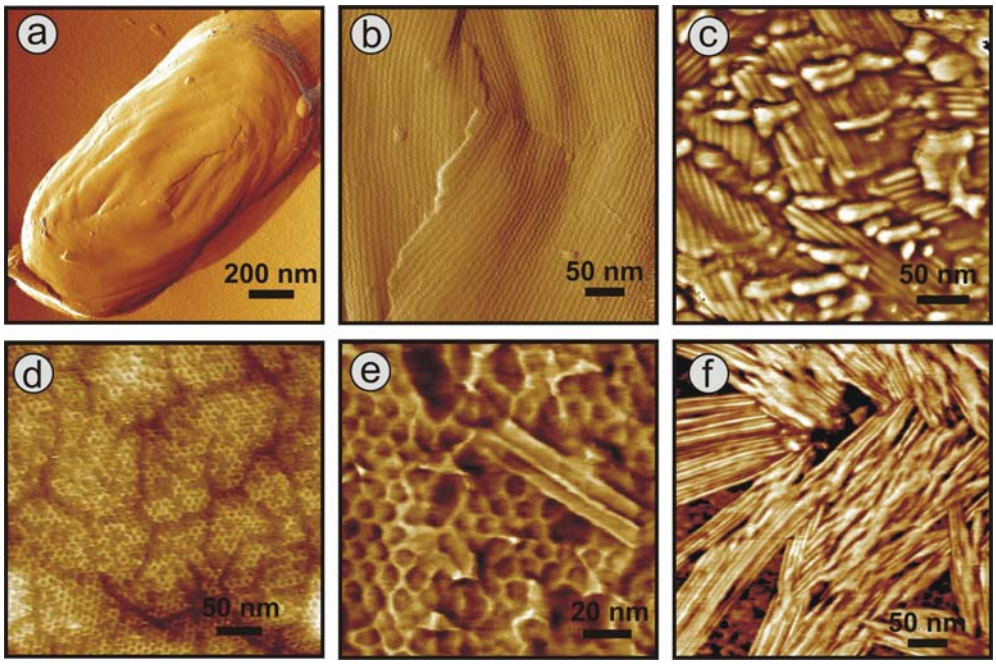

Figure 6. High resolution spore coat structures of *Bacillus spores*. The outer spore coats of *B. atrophaeus* (a,b), *B. cereus* (d) and *B. thuringiensis* (e) consist of crystalline layers rodlet and honeycomb structures. *B. cereus* spores contain a crystalline honeycomb structure (d) beneath the exterior rodlet layer (c). *B. thuringiensis* spore coats do not contain rodlet structures. Rodlet assemblies can be seen adsorbed to the substrate (f).

The ~ 10 nm thick rodlet layer of *B. cereus* spores is formed by multiple randomly oriented domains, comprised of parallel subunits with a periodicity of ~ 8 nm. The size of the domains is typically 100 – 200 nm. In contrast to the multi-domain rodlet structure of the *B. cereus* spore coat (Fig.6c), typically only a single continuous domain was found to be present on the outer coat of *B. atrophaeus* and *B. subtilis* spores. Multiple rodlet domains are less common. Generally, the main domain covers 60% – 100% of the spore surface, while 0% - 40% is covered by 0 – 10 smaller domains.[3] Complete removal of the exterior *B. cereus* rodlet layer by sonication revealed an underlying honeycomb structure (Fig. 6e) similar to the exterior spore coat layer of *B. thuringiensis* (Fig. 6d). For both species, the lattice parameter for the honeycomb structure is ~ 9 nm, with ~5 – 6 nm holes/ pits (Fig.6d,e). In case of *B. thuringiensis* spores, rodlet structures were not observed as an integral component of the spore coat;[1,3] however, as illustrated in Fig. 6f, patches of extrasporal rodlet structures were observed adsorbed to the substrate.[1,3] Rodlet width and thickness (Fig. 6e) were similar to those observed for *B. atrophaeus, B.subtilis* and *B. cereus* spore coat structures (Fig. 6a-c), which indicates that the similar rodlet proteins could be present during the sporulation in these three species of *Bacillus* spores.

Similar rodlet and honeycomb crystalline structures to those seen in Figure 6, were observed in freeze-etching EM studies of several species of *Bacillus* spores[32,40] and AFM studies of fungal spores.[45] Note, that in the case of *B. thuringiensis*, spore coat rodlet structures were not observed in freeze-etching EM.[32, 40]

Very little is known about the assembly, physical properties and proteomic nature of these bacterial spore rodlets. The closest structural and functional orthologs to the *Bacillus* species rodlet structure (*not* its protein sequence) are found outside the *Bacillus*

genus. Several classes of proteins, with divergent primary sequences, were found to form similar rodlet structures on the surfaces of cells of Gram-negative *Escherichia coli* and *Salmonella enterica* as well as spores of Gram-positive streptomycetes and various fungi (for the review see 46). Hydrophobins, a new class of structural proteins,[47] were shown to be necessary for and an integral component of rodlet fungal spore surface structures. Hydrophobins can self-assemble and produce layers of rodlet structures at water-air interfaces.[47] Fungal hydrophobin rodlet layers cause hyphal fragments and spores to become water-repellant, which enables escape from the aqueous environment and stimulates aerial release, dispersal and attachment to hydrophobic host surfaces.[46] However, while hydrophobin-like proteins are found in fungal spores, it has not been possible to identify orthologs of these proteins in bacterial spores.[48] These similarities in crystalline outer coat layer motifs found in prokaryotic and eukaryotic spore types are a striking and unexpected example of the convergent evolution of critical biological structures. Further investigation is required to determine the molecular composition of prokaryotic endospore rodlets and their evolutionary relationship to eukaryotic rodlet structures.

To observe the structure of the *C. novyi-NT* spore coat beneath the amorphous shell, we developed procedures to remove the shells by chemical treatment with various reducing agents and detergents or by physical treatment using a French Press.[8] When either French Press or chemical treatments were used, the majority of the exposed spore coat surface is formed by a ~ 8 - 10 nm thick honeycomb layer with a periodicity of 8.7 ± 1 nm (Fig. 7a).

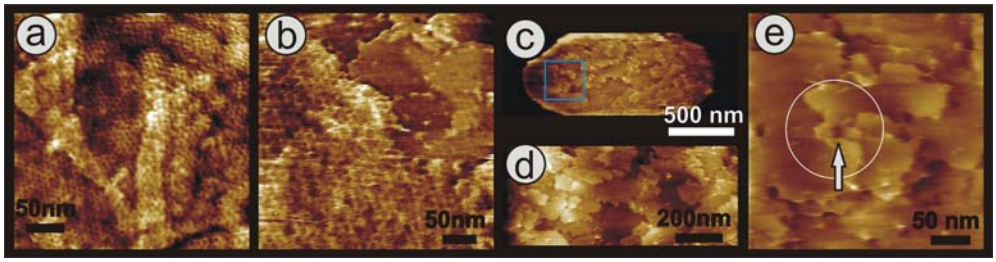

Figure 7. *C. novyi-NT* spore coats – high resolution AFM height images. (a) Removal of the amorphous shell by physico-chemical treatments reveals the underlying honeycomb layer with ~ 8.7 nm periodicity. (b) Most of the honeycomb layers disappeared from the spores within ~1 hr during the germination process. Remaining honeycomb patches (left, lower sides) could be easily removed by scanning with increased force. Below the honeycomb layer several underlying coat layers (upper right) are revealed. (c-e). Typical growth patterns seen on *C. novyi-NT* spore surface after removing the honeycomb layers. (c) Whole spore with several ~ 6 nm thick layers exposed on the surface. (d) Zoom-in of the center of (c) showing that spore coat layers originate at screw dislocations. (e) Zoom-in of the area indicated in (c). The circle in (e) denotes a four-fold screw axis. Many dislocation centers show depressions reminiscent of hollow cores (arrows), which are found in a wide range of crystals.

We have found that during the germination, the spores often had partly or completely lost their honeycomb layers, revealing the underlying layers (Fig. 7b). Note, that a number of spores, as judged by AFM observations, do not possess the amorphous layer. Furthermore, the presence of the amorphous material sandwiched between the spore coat and coat-associated honeycomb layers combined with the quick disappearance of these honeycomb layers during AFM germination experiments (Fig. 7),[8] all indicate that these *C. novyi-NT* honeycomb layers are not an integral part of the spore coat, as the 'rodlet layer' or 'honeycomb layer' is for *Bacillus* species (Fig.6)[1-3], but rather are a parasporal layer with an increased affinity for the spore coat.

As seen in Figure 7b-e, the removal of the honeycomb layer revealed a multilayer structure formed by ~ 6 nm thick smooth layers. Typically, there were 3 – 6 layers exposed on the spore surface. The spore coat surface patterns (Fig. 7b-e) were very similar to ones observed on the surfaces of inorganic, organic and macromolecular crystals.[49-52] As seen in Fig. 7b-e, these crystalline spore coat layers exhibited growth patterns typically observed on inorganic and macromolecular crystals. These patterns include steps and growth spirals originating from screw dislocations, such as those previously described in studies of the crystallization of semiconductors,[53] salts[54] and biological macromolecules.[51,52] In the middle of the growth centers, the dislocations cause depressions, typically < 15 nm, which are known as *hollow cores* in crystal growth theory and are formed by the stress associated with the dislocations.[55,56]

Thus the presence of the above mentioned growth patterns confirm crystalline nature of the coat layers. However, while AFM resolution is typically sufficient for visualization of crystal lattices on a molecular scale for a wide range of protein crystals,[52,57,58] we were not able to resolve a regular, crystalline lattice on the *C.novyi-NT* spore coat layers. Hence, the lattice periodicity is assumed to be smaller than ~1 nm, which is the resolution associated with the sharpest AFM tips used. Such a periodicity would be small compared to the 6 nm thickness of individual spore coat layers. In the case of globular proteins, lateral lattice parameters typically do not differ to such an extent from the height of growth layers, which is reflected in relatively small differences between lateral and perpendicular crystallographic unit cell parameters.[57] Thus, the proteins forming the *C. novyi-NT* crystalline spore coat layers are likely not globular, but rather may be stretched peptides 'standing upright' in the layers. This construction, which

is found in paraffin[50] and fat crystals[58], results in a crystal class with relatively strong, hydrophobic interaction forces between the long neighboring units (here peptides) and weak interaction forces between the different crystalline layers. This generally leads to wide, thin crystals that mainly grow laterally and can grow perpendicular only via the screw dislocation spiral mechanism (as was indeed seen for the *C. novyi-NT* coat layers). Such a crystal type, with tightly packed, strongly interacting longitudinal peptides within a layer, would help explain the toughness associated with bacterial spore coats.[24,40] It may also explain why spore coat proteins are difficult to dissolve,[24,40,59] as this type of packing involves hydrophobic interactions, and hence a high proportion of hydrophobic amino acids.

In addition to enabling the nucleation and growth of new coat layers during sporulation, the screw dislocations also pin several of these layers together, thereby making the spore coat an interconnected, cohesive entity, rather than a set of separate layers loosely deposited on top of each other. This, combined with the strong in-layer bonds, and possible cross-linking between the coat proteins, likely contributes to the resilient nature of the spore coat.

In biology, crystallization is most often associated with biomineralization, where protein-directed crystallization leads to calcious bone[60] and shell formation.[61,62] Screw dislocations and ensuing spiral growth have been observed for shell formation.[63,64] High-resolution scanning electron probe X-ray microanalysis[65,66] and nanometer-scale secondary ion mass spectrometry[67] studies have demonstrated that the proteinaceous coat of several bacterial spore species is essentially devoid of divalent mineral cations such as calcium, magnesium and manganese. This indicates that *C. novyi-NT* spores could

present the first case of non-mineral crystal growth patterns being revealed for a biological organism.

The implication for bacterial spore coat assembly is that, while the proteineous building blocks are produced via biochemical pathways directed by various enzymes and factors[24], the actual construction of these building blocks into spore coat layers is a self-assembly crystallization process Similarly, the striking differences in native rodlet motifs seen in *B. atrophaeus* (one major domain for each spore), *B. cereus* (a patchy multi-domain motif) and *B. thuringiensis* (extrasporal rodlets) appear to be a consequence of species-specific nucleation and crystallization mechanisms which regulate the assembly of the outer spore coat. In the case of *B. cereus* outer coat assembly, the surface free energy[68] for crystalline phase nucleation appears to be low enough to allow the formation of multiple rodlet domains resulting in cross-patched and layered assemblies. During the assembly of the outer coat of *B. atrophaeus* spores, the surface free energy may be considerably higher; reducing nucleation to the point that only one major domain is formed covering the entire spore surface. In addition to the possible differences in the surface free energies of the underlying inner coat, the pronounced difference in the nucleation rate of the outer coat rodlet layers for different *Bacillus* species could be caused by different supersaturation levels of the sporulation media during rodlet self-assembly.

Since the molecular mechanisms of self-assembly of spore coat structural layers appear to be very similar to those described for nucleation and crystallization of inorganic and macromolecular single crystals[51,52,68], fundamental and applied concepts developed for the nucleation and growth of inorganic and protein crystals can be applied

successfully to understanding the assembly of the spore coat. Thus based on experimentally observed rodlet structural properties, we have developed a model for rodlet spore surface assembly, which was derived from well-developed molecular-scale crystallization/self-assembly mechanisms.[3]

The consequence of spore coat crystalline assembly process is that the spore coat is not only influenced by the biochemical pathways leading to the production of spore coat proteins, but also by the crystallization conditions during which these proteins assemble themselves. By analogy to 'regular' protein crystallization, conditions during sporulation such as salt concentration, pH, the presence of impurities, nucleation rates of crystalline self-assembly of spore coat layers, and random variations in the number of screw dislocations on spores could change the growth rate and hence the thickness of the spore coat. This in turn could influence characteristics such as the resilience of spores, their lifetime, and their germination capacity.

Furthermore, these observations suggest that spore coat architecture and assembly are not only genetically determined, but could be also strongly influenced by the modifications of sporulation media, which in turn could affect spore germination competence and physicochemical properties. However, the effects of environmental and chemical perturbations on spore coat structure have not been systematically investigated. Thus, under different sporulation conditions, it is possible that rodlets could nucleate and assemble on the outer coat of *B. thuringiensis* spores instead of self assembling in bulk media, as described above (Fig. 6e).

By observing spore coat high-resolution structures, AFM analysis could be utilized to reconstruct the environmental conditions that were present during spore

formation. In order to explore our hypothesis on the production-specific self-assembly of the spore coat, we have conducted AFM experiments on the characterization of the spore coat of *B. thuringiensis* spores grown under different sporulation conditions. Spore preparations grown in Nutrient Broth (NB) and G media were analyzed. For spores grown in NB media, only honeycomb crystalline layer were seen (Fig. 8a,b) on the spore coat of *B. thuringiensis,* similar to our previous results. In our previous experiments only extrasporal rodlets were found in preparations of *B. thuringiensis* spores (2). We have suggested (2) that variations in sporulation conditions could allow rodlets to nucleate,

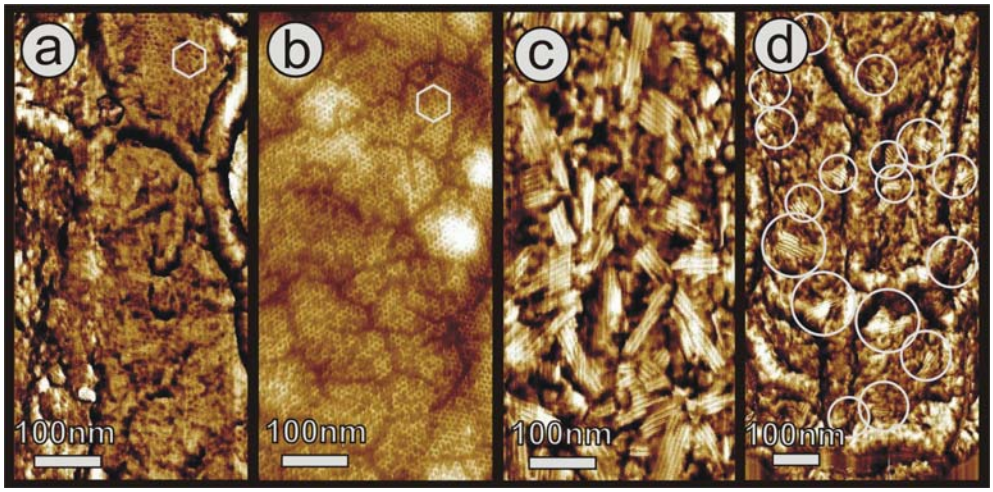

Figure 8. AFM images showing the outer coat structure of *B. thuringiensis* spores grown in NB media (a,b) and G media (c,d). Honeycomb and rodlet crystalline structures are indicated with hexagons (a,b) and circles (d) respectively.

assemble and attach to the outer coat of *B. thuringiensis* spores instead of being present in bulk media as extrasporal rodlets. This case was observed for spore samples grown in G medium (Fig. 8, c,d). Both for solution- and agar-grown (G medium) spores, patches of rodlet structure were visualized on the spore coat of air-dried and fully hydrated spores. It

appears that these rodlet structures are directly correlated to differences in the medium conditions during sporulation.

Through systematic sampling (data are not shown here), it was found that rodlet patches are present on all of the spores grown in G medium. On the other hand, none of the spores, grown in NB medium contained rodlet structure patches. These data establish that outer coat structural motifs (patches of rodlet crystalline structures) are directly correlated to differences in the medium conditions during sporulation. These findings validate that AFM can identify formulation-specific structural attributes that could be used in bioforensics to reconstruct spore formulation conditions.

Unraveling of the spore coat assembly with AFM-based immunolabeling. AFM provides high-resolution topographical information about the spatial and temporal distribution of macromolecules in biological samples. However, simultaneous near molecular-resolution topographical imaging of biological structures and specific recognition of the proteins forming these structures is currently lacking. Of particular importance is the identification of the protein composition of pathogen surfaces. Pathogen outer surface structures (e.g. virus membranes and capsids, as well as bacterial cell walls, spore coats and exosporia) typically contain multiple proteins. While it is known to a certain degree which proteins are expressed for these surface structures, it is often unknown which of these are exposed on the outside of these structures and which are embedded within the structures. Detection of surface-exposed proteins is paramount for improving the fundamental understanding of their functional properties as well as for the development of detection, attribution and medical countermeasures against these

pathogens. In the past several years, considerable progress, in particular towards probing of microbial and cellular systems, has been made in identification and mapping of specific receptors and ligands on the biological surfaces using adhesion force mapping and dynamic recognition force mapping (for reviews, see ref. 69,70).

Electron microscopy (EM)-based immunolabeling techniques have become an important tool for the elucidation of biological structure and function.[71,72] AFM immunogold markers were utilized in the past for imaging of proteins, macromolecular ensembles and protein-protein interactions.[73-79] We have recently utilized[5] AFM-based immunochemical labeling procedures for visualization and mapping of the binding of antibodies, conjugated with nanogold particles, to specific epitopes on the surfaces of *Bacillus anthracis* and *Bacillus atrophaeus* spores. In this study, we have established the validity (strength of antigen-antibody binding and avidity) of immunochemical labeling of the exosporium of *Bacillus anthracis* and the spore coat of *Bacillus atrophaeus* spores through various control experiments. We have further established the immunospecificity of labeling, through the utilization of specific anti-*B. atrophaeus and B. anthracis* polyclonal and monoclonal antibodies, which were targeted to spore coat and exosporium epitopes (Fig.9). In particular, we have confirmed that bclA glycoprotein is the immuno-dominant epitope on the surface of *B. anthracis* spores.[5]

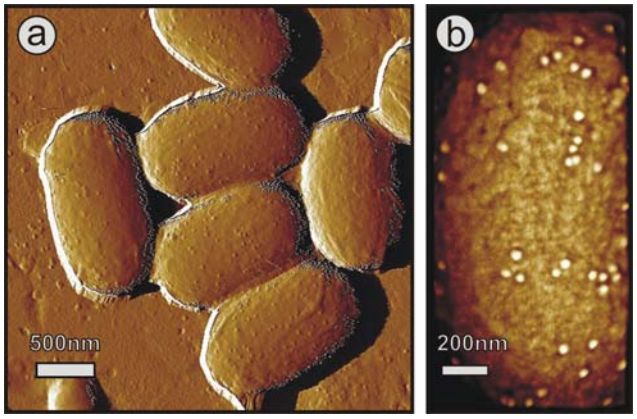

Figure 9. AFM images of specific binding of anti-*B. anthracis* gold-labeled polyclonal antibodies to the *B. anthracis* spore exosporia.

Spore coat assembly. Proper assembly of a multilayer spore coat of *Bacillus* spores is dependent on a number of coat proteins.[24] Loss of any of those proteins could alter significantly the mechanisms of the spore coat assembly and the final spore coat structure. Indeed, as demonstrated in Figure 10, deletion of a single spore coat protein could result in pronounced changes in the spore coat architecture.[7] Thus, the AFM

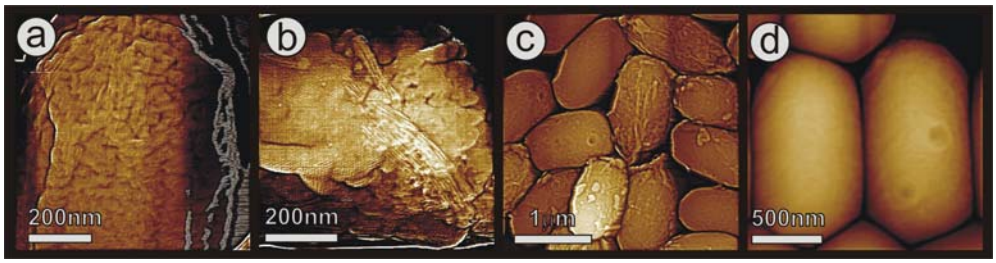

Figure 10. AFM images of *B. subtilis* spores of different strains. The spores analyzed were wild-type (a), *cotE* (b), *gerE* (c), and *cotEgerE* (d).

analysis showed[6] that intact wild-type spores are completely or partially covered by a thin amorphous layer lacking defined structure (Fig. 10a). Directly below the amorphous layer is a rodlet crystalline layer (Fig. 10a), which has parameters similar to the *B. atrophaeus* rodlet spore coat layer.[3] *CotE* is a major spore coat morphogenetic protein, and in its absence the outer coat fails to assemble properly.[80] Indeed, we have demonstrated that for most (>90%) *cotE* spores the outermost structure is formed by 3-5 crystalline layers, each of which is ~6 nm thick (Fig. 10b), which are likely correspond to the inner coat layers, as is the case for the coats of *Clostridium novyi* (Figure) spores.[8] Note that remnants of small patches of rodlet structures or groups of several individual rodlets were seen on the majority of *cotE* spores (Fig. 10b). Furthermore, surfaces of some *cotE* mutant spores exhibit patches or large regions covering the spore of a hexagonal crystalline layer (located between the rodlet layer and the inner coat multi-

layer structure) (Fig. 10b). Surfaces of *gerE* spores were found to lack completely both amorphous and rodlet structures, being encased in several inner spore coat layers.[7] Note that the number of inner coat layers were found to be less on *gerE* spores compared to *cotE* spores. Finally, spores lacking both *CotE* and *gerE* proteins (*cotEgerE* spores) were found to lack all outer and inner coat structures.[7] The outer surface of *CotEgerE* spores was found to be quite smooth and corresponds likely to the spore cortex, which is typically located in wild type spores under the multilayer spore coat structure (Fig.1). Our recent comprehensive analysis of a wide range of *B. subtilis* mutants, which lack various spore coat proteins (data are not presented here) here, have provided improved understanding of the spore coat architecture and assembly.

Mechanisms of spore germination.

Upon exposure to favorable conditions, metabolically dormant *Bacillus* and *Clostridium* spores break dormancy through the process of germination[81-83] and eventually reenter the vegetative mode of replication. A comprehensive understanding of the mechanisms controlling spore germination is of fundamental importance both for practical applications related to the prevention of a wide range of diseases by spore-forming bacteria (including food poisoning and pulmonary anthrax), as well as for fundamental studies of cell development. Germination involves an ordered sequence of chemical, degradative, biosynthetic and genetic events. [81,83]

While significant progress has been made in understanding the biochemical and genetic bases for the germination process[81], the role of the spore coat in the germination remains unclear.[24,81] Spore coat structure regulates the permeation of germinant

molecules.[84,85] It is believed that penetration of germinants proceeds through pores in the coat structure and may involve GerP proteins.[85]

We have recently developed[4,8] in *vitro* AFM methods for molecular-scale examination of spore coat and germ cell wall dynamics during spore germination and outgrowth. To obtain a comprehensive understanding of the role of the spore coat in germination, AFM imaging on a nanometer scale is required. At this scale, the outer layer of the *B. atrophaeus* spore coat is composed of a crystalline rodlet array (Fig. 6a,b; Fig 11a) containing a small number of point and planar (stacking fault) defects.[3] Upon

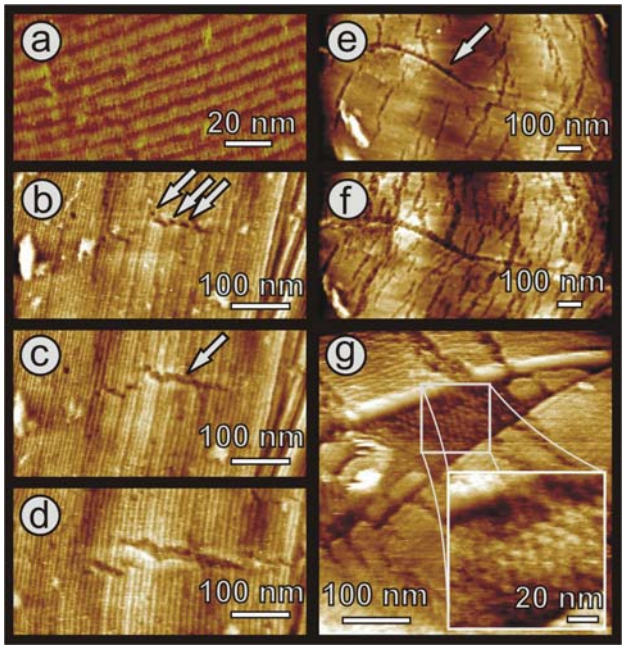

Figure 11. Disintegration of the spore coat layer. (a) The intact rodlet layer covering the outer coat of dormant *B. atrophaeus* spores is ~ 11 nm thick, and has a periodicity of ~ 8 nm (1-3). (b-d) Series of AFM images tracking the initial changes of the rodlet layer after (b) 13 min., (c) 113 min., and (d) 295 min. of exposure to germination solution. Small etch pits (indicated with arrows in b) evolve into fissures (indicated with an arrow in c) perpendicular to the rodlet direction. The fissures expand both in length and width. (e-f) Series of AFM images showing another germinating spore. The spore long axis, as well as major rodlet orientation is left-right. Enhanced etching at stacking faults (running from left to center and indicated with an arrow in e), as well as increased etching at the perpendicular fissures were visible

following (e) 135 min. and (f) 240 min. of germination. Fissure width and length increased from 10 – 15 nm and 100-200 nm (135 min.) to 15 – 30 nm and 125-250 nm (240 min.), respectively. (g) Etching and/or fracture of the rodlet layer at a stacking fault revealed the underlying hexagonal layer of particles with a 10-13 nm lattice period.

exposure to the germination solution, disassembly of the rodlet structures was observed.[4] During the initial stages of germination, the disassembly was initiated through the formation of 2-3 nm wide micro etch pits in the rodlet layer (Fig. 11b). Subsequently, the etch pits formed fissures (Fig. 11b-11d) that were, in all cases, oriented perpendicular to the rodlet direction. Simultaneously, etching commenced on the stacking faults (Fig. 11e-1f) revealing an underlying hexagonal inner spore coat layer (Fig. 11g). Note that the hexagonal layer was previously observed[6] beneath the rodlet layer on *B. subtilis* spores (Fig. 10b). During later stages of germination, further disintegration of the rodlet layer (Fig. 11e-11f) proceeded by coalescence of existing fissures, their autonomous elongation (at a rate of ~ 10 - 15 nm/hr) and widening (at ~ 5 nm/hr), and by continued formation of new fissures.

Disassembly of the higher-order rodlet structure began prior to the outgrowth stage of germination (Fig. 12). Disaggregation of the rodlet layer occurred perpendicular to the orientation of individual rodlets resulting in the formation of banded remnants (Fig. 12). Further structural disruption led to the formation of extended, 2 - 3 nm wide, fibrils (indicated with arrows in Fig. 12e) which were also oriented perpendicular to the rodlet direction.

The AFM studies presented here elucidate the time-dependent structural dynamics of individual germinating spores and reveal previously unrecognized nano-structural

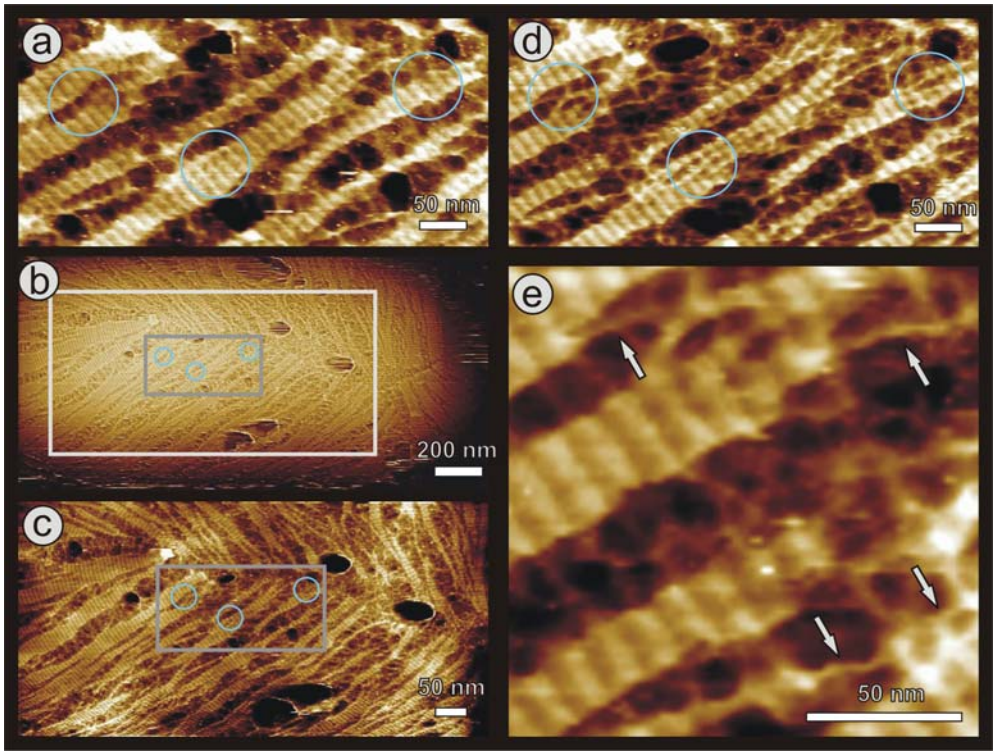

Figure 12. (a-d) Series of AFM height images showing the progress of rodlet disassembly. In the circled regions, banded remnants of rodlet structure (a) disassemble into thinner fibrous structures (d). Time between images was 36 min. (a) - (b); 3 min. (b)-(c) and 6 min. (c) - (d), for a total time between (a) and (d) of 45 min. In (b), the area imaged in (c) is indicated with a light grey box. In (b) and (c) the area imaged in (a) and (d) is indicated with a dark grey box. In (e), which is an enlarged part of (d), arrows indicate the end point of rodlet disruption, i.e. fibrils with a diameter of 2 – 3 nm, oriented roughly perpendicular to the rodlets.

alterations of the outer spore coat. Disassembly of the higher-order rodlet structure initiates at micro-etch pits, and proceeds by the expansion of the pits to form fissures perpendicular to the rodlet direction. What causes this breakdown of the rodlet layer?

We proposed[4] that rodlet structure degradation is caused by specific hydrolytic enzyme(s), located within the spore integument and activated during the early stages of germination. The highly directional rodlet disassembly process suggests that coat degrading enzymes could be localized at the etch pits, and either recognize their structural features, or that the etch pits are predisposed to structural deformation during early stages of spore coat disassembly. The gradual elongation of the fissures, suggests that once hydrolysis is initiated at an etch pit, processive hydrolysis propagates perpendicular to the rodlet direction and to neighboring rodlets.

The locations of the small etch pits may coincide with point defects in the rodlet structure. These point defects could be caused by misoriented rodlet monomers or by the incorporation of impurities into the crystalline structure. In both cases, point defects could facilitate access of degradative enzymes to their substrate in an otherwise tightly packed structure.

Recent proteomic and genetic studies suggest that the inner and outer spore coats of *Bacillus subtilis*, which is closely related to *Bacillus atrophaeu*s, are composed of over 50 polypeptide species.[24] However, it is unknown which of these proteins form the surface rodlet layer of the spore coat or how this outer spore coat layer is assembled. We have shown previously for *B. cereus*[1] *and B. subtilis*[7] spores and here for *Bacillus atrophaeu*s spores (Fig. 11g) that the outer spore coat rodlet layer is underlain by a crystalline honeycomb structure.

Several classes of proteins, with divergent primary sequences, were found to form similar rodlet structures on the surfaces of cells of Gram-negative *Escherichia coli* and *Salmonella enterica* as well as spores of Gram-positive streptomycetes and various

fungi.[46] These rodlets were shown to be structurally highly similar to amyloid fibrils.[46] Amyloids possess a characteristic cross β-structure and have been associated with neural degenerative diseases (*i.e.,* Alzheimer's and prion diseases).[86] Amyloid fibrils or rodlets form microbial surface layers[46], which play important roles in microbial attachment, dispersal and pathogenesis. We have proposed[4] that the structural similarity of *B. atrophaeus* spore coat rodlets and the amyloid rodlets found on other bacterial and fungal spores suggests that *Bacillus* rodlets have an amyloid structure. AFM characterization of the nanoscale properties of individual amyloid fibrils has revealed that these self-assembled structures can have a strength and stiffness comparable to structural steel.[87] The extreme physical, chemical and thermal resistance of *Bacillus* endospores suggests that evolutionary forces have captured the mechanical rigidity and resistance of these amyloid self-assembling biomaterials to structure the protective outer spore surface.

Structural studies of amyloids have identified an array of possible rodlet assemblies, each consisting of several (2 or 4) individual cross- β-sheet fibrils, which are often helically intertwined.[46] The number of fibrils determines the diameter of the rodlet. Most amyloids resulting from protein-folding diseases, and some naturally occurring amyloids, form individual fibrils or disorganized rodlets networks.

In spore coats of *B. atrophaeus*, the higher-order rodlet structure is organized as one major domain of parallel rodlets covering the entire spore surface.[3] Rodlet domain formation requires there must be periodic bonds in the rodlet direction ("parallel bonds") as well in the direction perpendicular to it ("perpendicular bonds").[88] In the case of amyloid-like rodlets, the *intra*-rodlet, parallel bonds are known and consist primarily of hydrogen bonds associated with the cross-β sheets that form the backbone of the rodlet

fibrils. However, the nature of the perpendicular bonds, *i.e.* the *inter*-rodlet bonds that keep the rodlets tightly packed, is unknown. Interestingly, for *B. atrophaeus* the ratio of length (parallel to rodlet direction) and width (perpendicular to rodlet direction) of the rodlet domains is on average ~ 1, indicating that during formation of these domains, growth velocity was similar in both directions, and hence parallel and perpendicular bonds were similar in strength.

Based on these rodlet features, one might expect that during germination individual rodlets would detach or erode, leaving a striated pattern *parallel* to the rodlet direction. Surprisingly, striations *perpendicular* to the rodlet direction were observed (Fig. 12), and 2 – 3 nm wide fibrils *perpendicular* to the rodlet direction (Fig. 12e) were the culmination product of coat degradation. This result indicates that during germination, perpendicular rodlet bonds are stronger, or are more resistant to hydrolysis, than bonds parallel to the rodlet direction. Second, and most surprisingly, these perpendicular structures facilitate the formation, of 200-300 nm long fibers *perpendicular* to the rodlet direction.

It is unclear how microbial amyloid fibers form these perpendicular structures. One possibility is that during formation of the rodlet layer, both intra-rodlet parallel bonds and inter-rodlet perpendicular bonds form, similar in strength and leading to tightly packed rodlets domains held together by a checkerboard-like bonding pattern. During germination, the intra-rodlet parallel bonds are hydrolyzed, while the inter-rodlet perpendicular bonds remain intact over longer time periods. Spore coat hydrolytic enzymes could target a specific residue or structure (in this case, that of the cross-β sheets) and leave other (here, perpendicular) residues or structures intact. Identification of

the gene(s) encoding the rodlet structure and the enzymes responsible for rodlet degradation are important areas for future research.

Although *in vitro* AFM is a surface imaging technique, internal structural changes that are physically separated from the probe tip by the thin rodlet layer could be visualized, much as the arrangement of ribs beneath the skin is apparent to a finger passing over them, or, as in other AFM applications, the visualization of the cytoskeleton network beneath the surface of the cell.[89] During early stages of the germination process, movement of 2-10 nm steps beneath the rodlet structure was consistently recorded (Fig. 13 a-d), which resulted in the formation of a pronounced ring structure beneath the outer

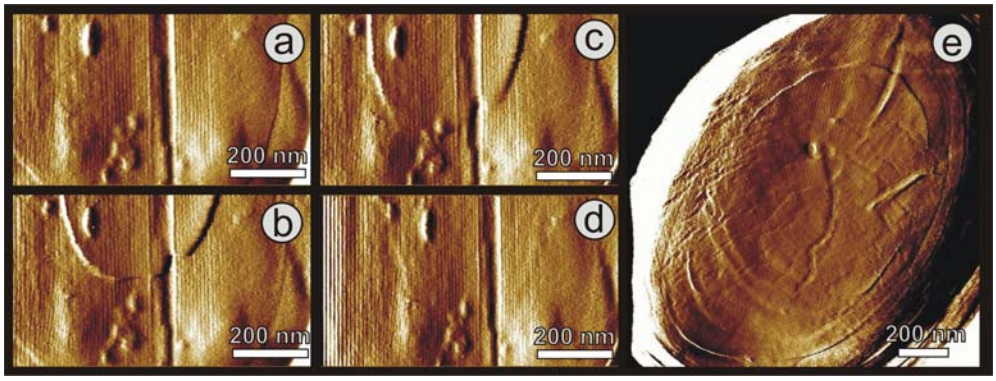

Figure 13. (a-d) Series of sequential AFM amplitude images showing passage of sub-surface steps during the early stages of germination. The central step visible in (a,b) has a height of 18 nm and a velocity of ~ 10 nm/s. Scan direction is down (a,c), up (b,d); time between images is 36 s. (e) AFM amplitude image showing sub-surface permanent ring structures, corresponding to a height difference of 4 – 8 nm, at 65 min. into germination. In general, observed step heights range from -10 to 0 to 25 nm, and velocities range from 0 – 100 nm/s.

spore coat surface (Fig. 2e). Moving steps were either ascending or descending with step velocities up to ~100 nm/s.

Emergence of vegetative cells. Etch pits were the initiation sites for early germination-induced spore coat fissure formation. During intermediate stages of germination, small spore coat apertures developed that were up to 70 nm in depth (Fig. 14b). During late stages of germination these apertures dilated (Fig. 14c-e) allowing vegetative cell emergence (data not shown).

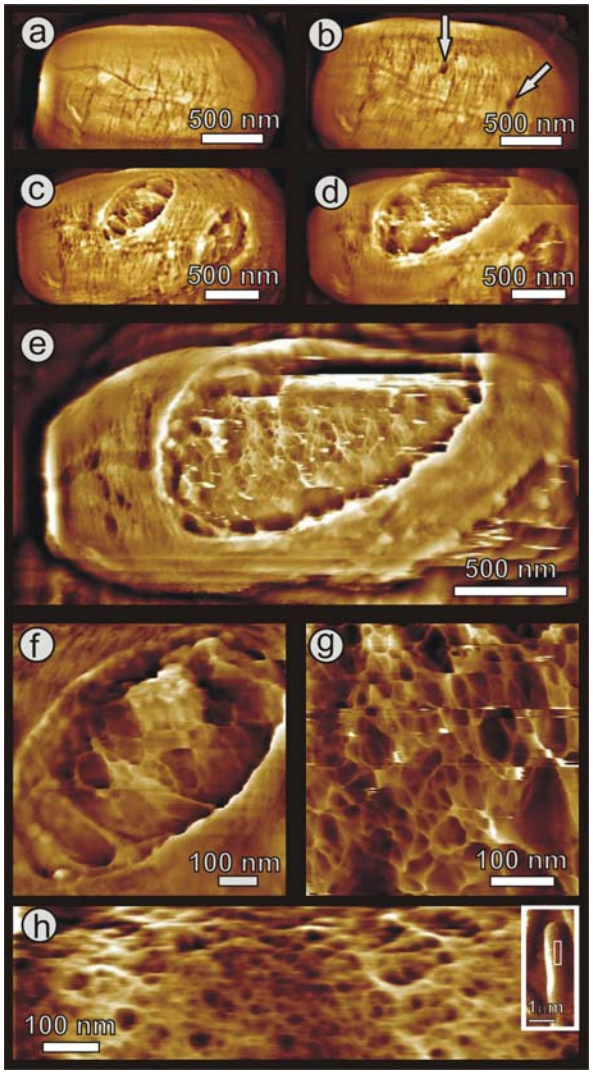

Figure 14. Emergence of vegetative cells. (a-g) Series of AFM height images showing 60-70 nm deep apertures in the rodlet layer (indicated with arrows in (b)) that gradually enlarged (c-d), and subsequently eroded the entire spore coat (e). Germ cells emerged from these apertures. (e) Prior to germ emergence from the spore coat, the peptidoglycan cell wall structure was evident. (f) At an early stage of emergence, the cell wall was still partly covered by spore remnants, while (g) immediately prior to cell emergence, the cell wall was free of spore integument debris. The germ cell surface contained 1 – 6 nm fibers forming a fibrous network enclosing pores of 5 – 100 nm. Images in (a-g) were collected on the same spore as those shown in Fig. 11e,f. Elapsed germination time (in hr:min) was (a) 3:40, (b) 5:45, (c)

7:05, (d) 7:30, (e) 7:45, (f) 7:15, (g) 7:50. (h) In separate experiments, cultured vegetative *B. atrophaeus* cells were adhered to gelatin surfaces and imaged in water. AFM height images show a slightly denser, similar fibrous network compared with the germ cell network structure (g), with 5 – 50 nm pores. In the inset, the imaged part (h) of the entire cell is indicated with a white rectangle.

In vitro AFM visualization of germling emergence allowed high resolution visualization of nascent vegetative cell surface structure (Fig. 14 e-g). Vegetative cell wall structure could be recognized through the apertures approximately 30-60 minutes prior to germ cell emergence. The emerging germ cell surface was initially partially covered with residual patches of spore integument (Fig. 14f). During the release of vegetative cells from the spore integument, the entire cell surface consisted of a porous fibrous network (Fig. 14g).

In order to compare the cell wall structure of germling and mature vegetative cells, we carried out separate experiments in which cultured vegetative *B. atrophaeus* cells were adhered to a gelatin-coated surface[4], and imaged with AFM in water. As seen in Fig. 14h, the cell wall of mature vegetative cells contained a porous, fibrous structure similar to the structure observed on the surface of germling cells (Fig. 14g).

The bacterial cell wall consists of long chains of peptidoglycan that are cross-linked via flexible peptide bridges.[91,92] While the composition and chemical structure of the peptidoglycan layer vary among bacteria, its conserved function is to allow bacteria to withstand high internal osmotic pressure.[91] The length of peptidoglycan strands varies from 3-10 disaccharide units in *S. aureus* to ~ 100 disaccharide units in *B. subtilis*, with each unit having a length and diameter of ~1 nm.[92] The fibrous network observed on the germ cell surface with 5 – 100 nm pores, (Fig. 14e, g), and the fibrous network observed

on mature vegetative cells with 5 – 50 nm pores (Fig. 14h) appear to represent the nascent peptidoglycan architecture of newly-formed and mature cell wall, respectively, and is comprised of either individual or several intertwined peptidoglycan strands. The cell wall density of mature cells appears to be higher with, on average, smaller pores and more fibrous material, as compared to the germ cells. These results are consistent with murein growth models whereby new peptidoglycan is inserted as single strands and subsequently cross-linked with preexisting murein.[93] The AFM-resolved pore structure of the nascent *B. atrophaeus* germ and vegetative cell surfaces is similar to the honeycomb structure of peptidoglycan oligomers determined by NMR.[91]

Note, the AFM data presented here suggests that peptidoglycan structure rearrangement may occur prior to the formation of the fibrous cell wall network. As seen in Figure 13, during the early stages of germination, movement of 0 - 25 nm steps beneath the outer spore coat and formation of pronounced ring structures occurred. Similar concentric rings were observed by EM[94] and AFM[95] in newly divided Gram-positive cell walls. It was suggested[95] that these rings were caused by peptidoglycan structural rearrangements during cell division. The rings and steps observed during the early stages of germination could be caused by peptidoglycan restructuring that accompanies maturation of the nascent sacculus.[96]

The structural dynamics of *C. novyi-NT*[8] and *B. atrophaeus* germinating spores appears to be similar. Thus, at later stages of the germination process, the *C. novyi-NT* spore coat layers seen in Fig. 15 , which are exposed at early stages of germination start to dissolve (Fig. 15). Thus this process was initiated by the formation of fissures (Fig. 15a), which subsequently widened and elongated (Fig. 15b-e), resulting in isolated

islands of remnant coat layers (Fig. 15e,f). The dissolution of coat layers revealed an underlying undercoat layer (marked with arrows in Fig. 15e).

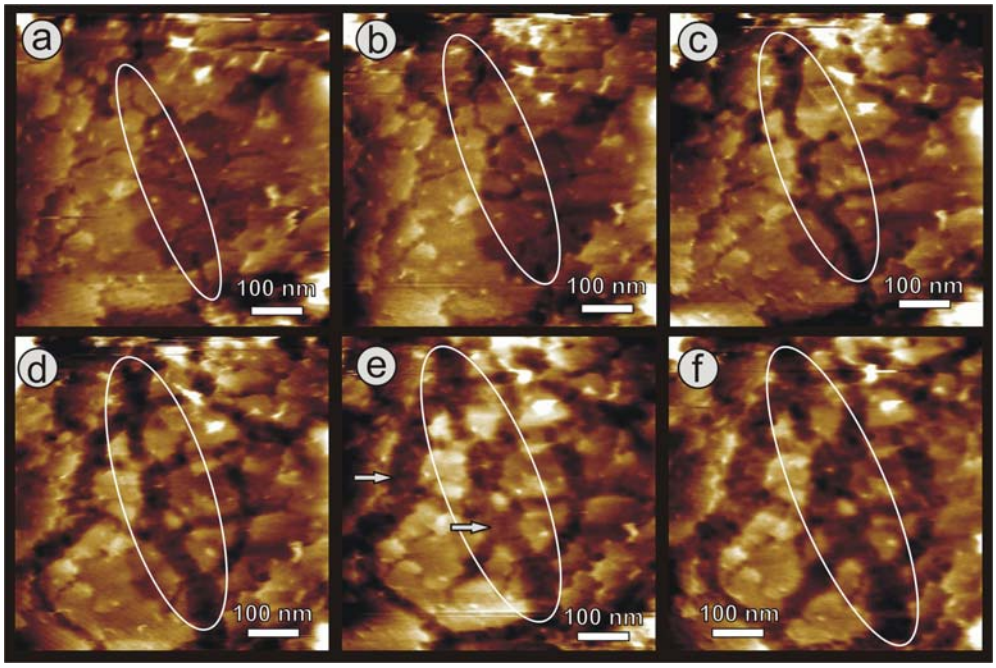

Figure 15. Dynamic AFM height imaging of degrading *C. novyi-NT* spore coat layers. Fissures first appeared (a,b), then laterally expanded into wide gaps (c-e) and eventually resulted in the removal of whole layers, exposing the underlying layer (e,f, arrows in (e)). One expanding fissure is indicated with a white oval in (a-f). Time in germination medium in hr:min was 0:45 (a), 0:50 (b), 0:55 (c), 1:00 (d), 1:05 (e), 1:10 (f).

Similarly to *B. atrophaeus* spore germination mechanisms described above, coat degradation likely occurs under the influence of germination-activated lytic enzymes. In fact, such lytic enzymes are known to be encoded within the *C. novyi-NT* genome.[97] Interestingly, *C. novyi-NT* spores contain mRNA, and these mRNA molecules are enriched in proteins that could assist with cortex and other degradation.[97]

At the final stages of germination, the coat layers dissolved completely (Fig. 16a), fully exposing the ~ 20-25 nm thick undercoat layer. In the following stage of germination this layer also disintegrated. This proceeded through the formation and slow expansion of ~ 25 nm deep flat-bottomed apertures (Fig. 16a-f). The cortex was fully lysed by the time spore coat layers dissolved. Hence, the flat-bottomed apertures in this undercoat layer show the underlying cell wall of the emerging *C. novyi-NT* vegetative cell, which, based on its lighter AFM phase contrast (Fig. 16f), has different physicochemical properties or/and hence, composition than the surrounding coat remnants. The nascent surface of the emerging germ cell appears to be formed by a porous network (Fig. 16e-f) of peptidoglycan fibers, similar to one described above for *B. atrophaeus* vegetative cells (Fig. 14g,h).

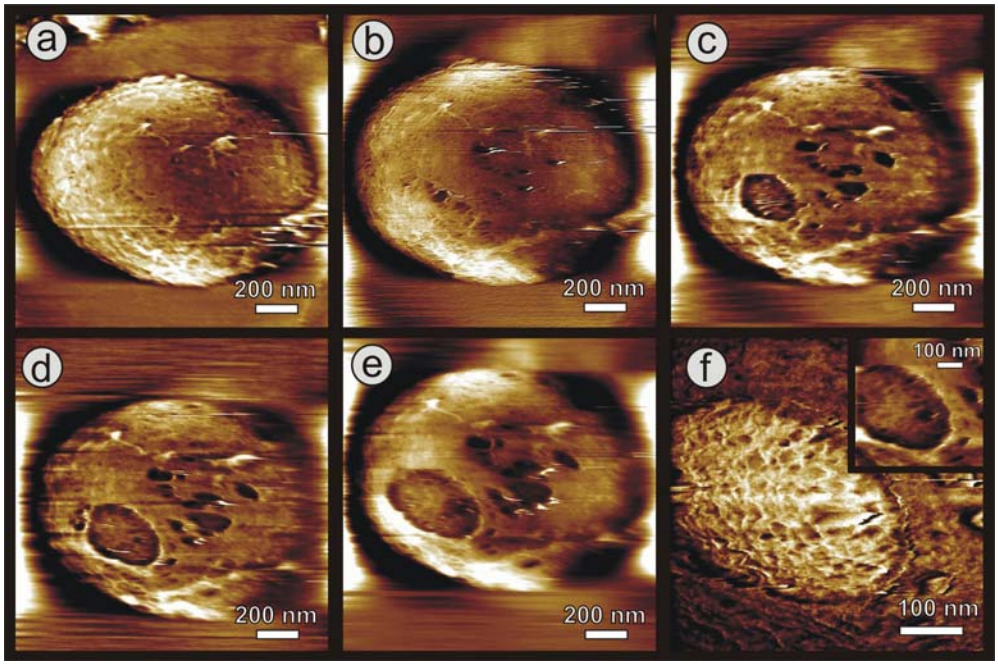

Figure 16. (a – e) AFM height images of the final outgrowth stage. (a) After the ~6 spore coat layers were largely dissolved, the underlying structural layer was exposed. (b-e) In

this layer, 25 nm deep apertures appeared and grew laterally. (f) Phase image zoom-in of the largest aperture depicted in (c-e), showing the pronounced phase contrast, indicating the different material properties of the emerging cell wall (light) and remaining spore layer (dark). Inset in (f) is the concurrent height image, showing the 25 nm deeper position of the cell wall with respect to the surrounding spore layer. Time in germination medium in hr:min was 1:40 (a), 2:15 (b), 2:50 (c), 3:35 (d), 3:50 (e), 3:55 (f).

Note that the spore coat degradation process presented in Figs. 11-16 appears not to be affected by the scanning AFM tip.[4,8] The shapes of fissures and apertures remained unaltered after repeated scanning. Furthermore, when we zoomed out to a larger previously non-scanned area after prolonged scanning on a smaller spore area, the initially scanned area did not display any tip-induced alterations (such as a larger degree of coat degradation). Finally, when we did not image spores for more than an hour between two scans, the coat degradation pattern had developed similarly when compared to spores that were scanned continuously.

Spore germination provides an attractive experimental model system for investigating the genesis of the bacterial peptidoglycan structure. Dormant spore populations can be chemically cued to germinate with high synchrony[81], allowing the generation of homogenous populations of emergent vegetative cells suitable for structural analysis.

Proposed models for the bacterial cell wall structure posit that peptidoglycan strands are arranged either parallel (planar model) or orthogonal (scaffold model) to the cell membrane.[90,91] Existing experimental techniques are unable to confirm either the planar or the orthogonal model. The experiments described here do not contain sufficient high-resolution data, in particular of individual peptidoglycan strands, to deduce with

certainty the tertiary three-dimensional peptidoglycan structure. The pore structures (Fig.14,16) of the emergent germ and mature vegetative cell wall - an array of pores - suggest a parallel orientation of glycan strands with peptide stems positioned in stacked orthogonal planes.[91] More detailed studies of germ cell surface architecture and morphogenesis will be required to confirm this peptidoglycan architecture and to investigate whether glycan biosynthesis precedes peptide cross-linking.

The results presented here demonstrate that *in vitro* AFM is a powerful tool for revealing the structural dynamics and architectural topography of the microbial and cellular systems. AFM allows new approaches to high-resolution real-time dynamic studies of single microbial cells under native conditions. Environmental parameters (ex., temperature, chemistry or gas phase) can be easily changed during the course of AFM experiments, allowing dynamic environmental and chemical probing of microbial surface reactions. Further incorporation of AFM-based immunolabeling techniques described above, could allow the identification of spore coat proteins that play a role in spore germination, and provide a structural understanding of how these proteins regulate spore survival, germination and disease.

Bacteria-mineral interactions on the surfaces of metal-resistant bacteria. We are currently conducting studies on the elucidation of bioremediation mechanisms of *Arthrobacter oxydans* metal-resistant bacteria. *A. oxydans* is a gram-positive and chromium (VI)-resistant bacterium, which can reduce highly mobile, carcinogenic, mutagenic, and toxic hexavalent chromium to less mobile and much less toxic trivalent chromium. Toxic compounds and heavy metals can be removed from contaminated cites or waste by chemical and physical techniques, which are both difficult and expensive.

The extraordinary ability of indigenous microorganisms, like metal-resistant bacteria, for biotransformation of toxic compounds is of considerable interest for the emerging area of environmental bioremediation. However, the underlying mechanisms by which metal-resistant bacteria transform toxic compounds are currently unknown and await elucidation. Stress response pathways are sure to play an important role in the niche definition of metal-resistant bacteria and their effect on the biogeochemistry of many contaminated environments. The present technological and scientific challenges are to elucidate the relationships between the stress-induced organization and function of protein and polymer complexes at bacterial cell wall surfaces, to understand how these complexes respond to environmental changes and chemical stimulants, and to predict how they guide the formation of biogenic metal phases on the cell surface.

We have visualized air-dried *A. oxydans* bacteria and revealed the differences in surface morphology and flagella arrangements during different stages of bacterial growth. Thus, bacteria during the exponential stage growth (Fig. 17a) appear to have a rather smooth surface and show a peritrichous flagellar arrangement with flagella seen over the entire cellular surface. The surface of air-dried bacteria grown during the stationary phase (Fig.17b) appears to be tubular (Fig.17b, insert) and these bacteria show the lophotrichous flagellar arrangement with several flagella seen only at one pole of the cell.

We have further visualized for the first timestress responses of *A. oxydans* bacteria in response to the exposure to the toxic environment. Thus, as illustrated in Fig. 17c, the formation of a supramolecular crystalline hexagonal structure on the surface of *A. oxydans* bacteria exposed to 35-50 ppm Cr (VI) was observed. Since similar crystalline layers are not seen on control samples, this structure appears to be

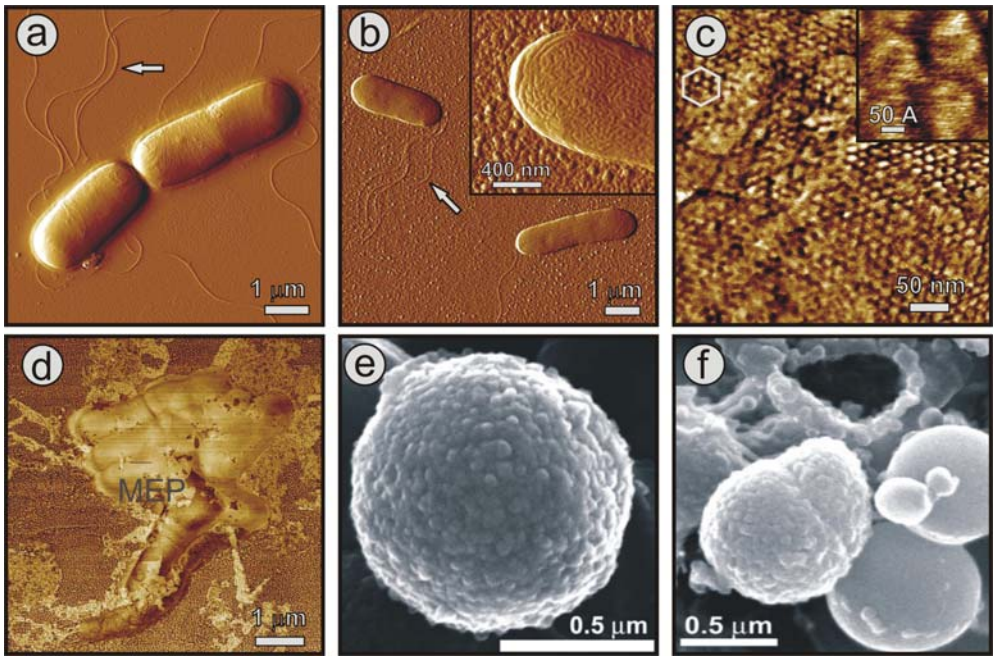

Figure 17. AFM images of *A. oxydans* bacteria. (a) and (b) growth dependent morphologies; (c) stress-induced supramolecular crystalline hexagonal layer on the bacterial surface; (d) stress-induced microbial extracellular polymers (MEP)layer covering a microbial colony. (e)-(f) SEM images of bacteria as a function of exposure time to Cr (VI). (e) 18 days; (d) 1 year.

stress-induced in response to Cr (VI) exposure. At higher Cr (VI) concentrations, we have observed the formation of microbial extracellular polymers (MEP), which are seen in Fig. 17d, to cover a small microbial colony.

Our AFM observations of the appearance of stress-induced layers on the surfaces of *A. oxydans* bacteria exposed to Cr (VI) are consistent with biochemical and electron microscopy (EM) studies of stress responses of *A. oxydans* bacteria. Thus, it was reported that *A. oxydans* grown with chromate concentrations above 40 mg/L significantly

increased the production of a cell wall protein that had an apparent molecular mass of 60 kDa.[98] Presumably, this protein could form, as seen in Fig.17c, a highly organized particulate layer on the surface of *A. oxydans* bacteria exposed to Cr (VI). The hexagonal stress-induced structure (Fig. 17c) is formed by a protein with the size of ~10-11 nm. High resolution images (Fig.17c, insert) reveal that these particles are oligomers, composed of monomers with a size of ~ 5 nm. Assuming the globular shape of the protein, this size corresponds well to the molecular mass of ~60KDa.

This 60 kDa protein was found to be positively charged and to act as an ion trap to bind negatively charged ions such as the soluble chromium anion $(CrO_4)^{2-}$[98] Indeed, scanning electron microscopy (SEM) images of *A. oxydans* exposed to 40-50 ppm of chromate clearly showed that the surface of *A. oxydans* grown with Cr(VI) was coated with an array of particles (Fig. 17e). These nanoparticles remained on the surface of *A. oxydans* for months before they were released into the immediate environment either individually or with other cell envelope materials as a shell (Fig. 17f), thereby maintaining basic vital processes such as growth and division, as well as nutrient transport.

We are currently developing procedures for *in vitro* high-resolution AFM characterization of the surface architecture, and structural dynamics of metal-resistant bacteria in response to changes in the environment and various chemical stimuli. It is expected that these experiments will improve the fundamental understanding of bioremediation mechanisms.

Acknowledgments

The authors thank B. Vogelstein, T.J. Leighton, P. Setlow and H.-Y. Holman for spore and bacteria preparations, and helpful discussions. This work was performed under the auspices of the U.S. Department of Energy by Lawrence Livermore National Laboratory under contract number DE-AC52-07NA27344. This work was supported by the Lawrence Livermore National Laboratory through Laboratory Directed Research and Development Grants 04-ERD-002 and 08-LW-027, and was funded in part by the Federal Bureau of Investigation.

References

1. M. Plomp, T.J. Leighton, K.E. Wheeler, and A.J. Malkin, Biophys. J. **88**, 603 (2005).

2. M. Plomp, T.J. Leighton, K.E. Wheeler, and A.J. Malkin, Langmuir **21**, 7892 (2005).

3. M. Plomp *et al.*, Langmuir **21**, 10710 (2005).

4 M. Plomp *et al.*, Proc. Nac. Acad. Sci. USA **104,** 9644 (2007).

5 M. Plomp and A.J. Malkin, Langmuir, in press (2009).

6. C. Monroe, M. Plomp, A.J. Malkin, and P. Setlow, Appl. and Environ. Microbiol. **74**, 5875 (2008).

7. S. Ghoshi *et al*., J. Bacteriol. **190**, 6741 (2008).

8. M. Plomp *et al.*, J. Bacteriol. **189**, 6457 (2007).

9. C.K. Cote *et al.*, in *Microorganisms and bioterrorism*, edited by M. Bendinelli, (Springer, New York 2006), pp. 83-111.

10. M. Mock and A. Fouet, Annu. Rev. Microbiol. **55,** 647 (2001).

11. F.A, Drobniewski,. Clin. Microbiol. Rev. **6**, 324 (1993).

12. D. Fritze and R. Pukall, Intl. J. of System. And Evolut. Microbiol. **51,** 35 (2001).

13. T.C.V. Penna, M. Marques, and I.A. Machoshvili, Appl. Biochem. And Biotech. **98,** 539 (2002).

14. S.A. Burke *et al*., Appl. and Environm. Microbiol. **70**, 2786 (2004).

15. D. P. Fergenson *et al.*, Anal.Chem. **2004**, 76, 373 (2004).

16. G. Vilas-Boas *et al*., Appl. Environ. Microbiol. **68**, 1414 (2002).

17. C.L. Hatheway, Microbiol. Rev. **3**, 66 (1990).

18. P. Bette *et al*., Infect. and Immun. **57**, 2507 (1989).

19. C. Bettegowda *et al*., Proc. Natl. Acad. Sci. USA **100**, 15083 (2003).

20. L. Van Mellaert, S. Barbé, and J. Anné, Trends Microbiol. **14**, 190 (2006).

21. L.H. Dang *et al*., Proc. Natl. Acad. Sci. USA **98**,15155 (2001).

22. N. Agrawal *et al***.,** Proc. Natl. Acad. Sci. USA **101**, 15172 (2004).

23. H.Y.N. Holman, D.L. Perry, and J.C. Hunter-Cevera, J. Microbiol. Meth. **34**, 59 (1998).

24. A. Driks, Microbiol.Mol.Biol.Rev. **63** 1 (1999).

25. A. Driks, A. and P. Setlow, in *Prokaryotic Development*, edited by Y.V. Brun and L.J. Shimkets (ASM Press, 2000) p.191.

26. Driks, A. *in Bacillus subtilis and its closest relatives*, edited by J.A. Hoch, J.A.; and R. Losik (ASM Press, 2002**)**, p.527.

27. J.J. Quinlan and M. Foegeding, Appl. Environ. Microbiol. **63**, 482 (1997).

28. K.Masuda, T. Kawata, K. Takumi, and T. Kinouchi, Microbiol. Immunol. **24**, 507 (1980).

29. L.L. Matz, T.C. Beaman, and P. Gerhardt, J. Bacteriol. **101**, 196 (1970).

30. M. Garcaia-Patrone and J.S. Tandecarz, Mol. Cell. Biochem. **145**, 29 (1995).

31. P. Gerhardt and E. Ribi, 1964. J. Bacteriol. **88,** 1774 (1964).

32. E. Wehrli, P. Scherrer, and O. Kubler, Europ. J. Cell Biol. 20**,** 283 (1980).

33. C. Redmond, L.W.J. Baillie, S. Hibbs, A.J.G. Moir, and A. Moir, Microbiology **150**, 355 (2004).

34. C.T. Steichen, J.F. Kearney, and C.L. Turnbough, Jr.,. J. Bacteriol. **187**, 5868 (2005).

35. P. Sylvestre, P., E. Couture-Tosi, and M. Mock, J. Bacteriol. **187**, 5122 (2005).

36. H. Kim *et al.*, Mol Microbiol. **59**, 487 (2006).

37. J. P. Desrosier and J.C.J. Lara, Gen. Microbiol. **130**, 935 (1984).

38. Y. Hachuka, S. Kozuka, and M. Tsujikawa,. Microbiol. Immunol. **28**, 619 (1984).

39.S. Kozuka and K.Tochikubo, Microbiol. Immunol. **29**, 21 (1985).

40. A.I. Aronson and P. Fitz-James, Bacteriol. Rev. **40,** 360 (1976).

41. V.G.R. Chada, E.A. Sanstad, R. Wang, and A. Driks, J. Bacteriol. **185**, 6255 (2003).

42. A. Driks, Proc. Natl. Acad. Sci. USA **100**, 3007 (2003).

43. A.J. Westphal, P. Buford Price, T.J. Leighton, and K.E. Wheeler. Proc. Natl. Acad. Sci. USA **100**, 3461 (2003).

44. H. Kim *et al.*, Mol. Microbiol. **59**, 487 (2006).

45. Y.F. Dufrêne *et al*., J Bacteriol. **181**, 5350 (1999).

46. M.F. Gebbink *et al.*, Nature Rev. Microbiol. **3**, 333 (2005).

47. J.G. Wessels, Adv. Microb. Physiol. **38**, 1 (1997).

48. T. J. Leighton, T., unpublished.

49. J.J. DeYoreo, T. A. Land, and B. Dair, Phys. Rev. Lett. **73**, 838 (1994).

50. M. Plomp, W. J. P. van Enckevort, P. J. C. M. van Hoof, and C. J. van de Streek, J. Cryst. Growth **249**, 600 (2003).

51. A.J. Malkin *et al*., Nature Struct. Biol. **2,** 956 (1995).

52. A.J. Malkin and A. McPherson, in *From solid-liquid interface to nanostructure engineering*, edited by X.Y. Lin, and J.J. DeYoreo vol. 2, pp. 201-238 (Plenum/Kluwer Academic Publisher, New York, NY., 2003).

53. B. Brar and D. Leonard, Appl. Phys. Lett. **66,** 463 (1994).

54. Maiwa, K., M. Plomp, W. J. P. van Enckevort, and P. Bennema, J. Cryst. Growth **186,** 214 (1998).

55. N. Cabrera and M. M. Levine, Philos. Mag. **1**, 450 (1956).

56. B. Van der Hoek, J. P. Van der Eerden, and P. Bennema. 1982. J. Cryst. Growth **56**, 621 (1982).

57. Yu. G. Kuznetsov *et al*., Biophys. J. **72**, 2357 (1997).

58. Hollander, F. F. A., M. Plomp, C. J. van de Streek, W. J. P. van Enckevort, Surf. Sci. **471**, 101 (2001).

59. H.-S. Kim, D. Sherman, F. Johnson, and A. I. Aronson, J. Bacteriol. **186**, 2413 (2004).

60. A. Veis, A.2003. in *Reviews in Mineralogy and Geochemistry*, edited by P. M. Dove, J. J. De Yoreo, and S. Weiner Vol. 54, (Mineralogical Society of America, Washington, D.C., 2003), p.249-289.

61**.** J. Aizenberg, G. Lambert, S. Weiner, and L. Addadi, J. Am. Chem. Soc. **124,** 32 (2002).

62. A.M. Belcher *et al*., Nature **38,** 56 (1996).

63. N. Yao, A. Epstein, and A. Akey, J. Mater. Res. **21**, 1939 (2006).

64. S.W. Wise and J. deVilliers, Trans. Am. Micro. Soc. **90,** 376 (1971).

65. K. Johnstone, D. J. Ellar, and T. C. Appleton, FEMS Microbiol. Lett. **7**, 97 (1980).

66. M. Stewart *et al*., J. Bacteriol. **143**, 481 (1980).

67. P. Weber, unpublished.

68. Chernov, A.A. Modern Crystallography III. Crystal Growth. Springer-Verlag: Berlin, 1984.

69. Y.F. Dufrêne and P. Hinterdorfer, P. Eur. J. Physiol. **256** 237 (2008).

70. Y.F. Dufrêne, Nature Microbiology Reviews **6**, 674 (2008).

71. J.M. Robinson, T. Takizawa, and D.J. Vandre, Microscopy **199**, 163 (2000).

72. M. Bendayan, Science **291**, 1363 (2001).

73. D. Kaftan *et al*., EMBO J. 21, 6146 (2002).

74. P. Soman, Z. Rice, and C.A. Siedlecki, Micron **39**, 832 (2008).

75. Lin,H.; Lal,R.; Clegg, D.O. Biochemistry **2000**, 39, 3192-3196.

76. C.A.J. Putman, B.G. de Grooth, P.K. Hansma, and N.F. van Hulst, Ultramicroscopy **48**, 177 (1993).

77. Y. Arntz *et al*.,. Microscopy Res. and Techn. **69**, 283 (2006).

78. D.J. Müller, C.-A. Schoenenberger, G. Büldt, and A. Engel, Biophys. J. **70**, 1796 (1996).

79. D. Alsteens *et al*., Eur. J. Physiol. **2008**, **456**, 117 (2008)

80. S. Little and A. Driks, Mol. Microbiol. **42**, 1107 (2001).

81. A. Moir, J. Appl Microbiol. **101**, 526 (2006).

82. A. Moir, B.M. Corfe, and J. Behravan, (2002) Cell Mol Life Sci. **59**, 403 (2002).

83. P. Setlow, (2003) Curr Opin Microbiol. **6**, 550 (2003).

84. A. Moir, B.M. Corfe, J. Behravan, Cell. Mol. Life Sci. **59**, 403 (2002).

85. J. Behravan, H. Chirakkal, A. Masson, and A. Moir, J. Bacteriol. **182**, 1987 (2002).

86. C.M. Dobson, Nature **426**, 884 (2003).

87. J.F. Smith *et al*., Proc Natl Acad Sci USA **103**, 15806 (2006).

88. R.F. Grimbergen *et al*., Acta. Cryst. **A 54**, 491 (1998).

89. Yu.G. Kuznetsov, A.J. Malkin, and A.McPherson, J. Struct. Biol. **120**, 180 (1997).

90. W.Vollmer and J.V. Höltje, J Bacteriol. **186**, 5978 (2004).

91. S.O. Meroueh *et al*., Proc. Natl. Acad. Sci. USA **103**, 4404 (2006).

92. J.B.Ward, (1973) Biochem. J. **133**, 395 (1073).

93. J.V. Höltje and C. Heidrich, Biochimie **83**, 103 (2001).

94. K. Amako and A. Umeda, J. Ultrastruct. Res. **58**, 34 (1977).

95. A. Touhami, M.H. Jericho, and T.J. Beveridge, J. Bacteriol. **186**, 328 (2004).

96. A.L. Koch, J. Mol. Microbiol. Biotechnol. **11**, 115(2006).

97. C. Bettegowda *et al*., Nature Biotech.**24**, 1573 (2006).

98. M.K. Abuladze *et al*., Fresenius Environ. Bull. **11**, 562 (2004).